Understanding variations in downwelling longwave radiation using Brutsaert's equation

Yinglin Tian[1,2], Deyu Zhong[1], Sarosh Alam Ghausi[2,3], Guangqian Wang[1], Axel Kleidon[2]

[1]State Key Laboratory of Hydroscience and Engineering, Department of Hydraulic Engineering, Tsinghua University, 100084 Beijing, China.
[2]Biospheric Theory and Modelling, Max Planck Institute for Biogeochemistry, 07701 Jena, Germany
[3]International Max Planck Research School on Global Biogeochemical Cycles (IMPRS-gBGC), 07701 Jena, Germany

Correspondence to: Axel Kleidon (akleidon@bgc-jena.mpg.de)

Abstract

A dominant term in the surface energy balance and central to global warming is downwelling longwave radiation (R_{ld}). It is influenced by radiative properties of the atmospheric column, in particular by greenhouse gases, water vapour, clouds and differences in atmospheric heat storage. We use the semi-empirical equation derived by Brutsaert (1975) to identify the leading terms responsible for the spatial-temporal climatological variations in R_{ld}. This equation requires only near-surface observations of air temperature and humidity. We first evaluated this equation and its extension by Crawford and Duchon (1999) with observations from FLUXNET, the NASA-CERES dataset, and the ERA5 reanalysis. We found a strong spatiotemporal correlation between estimated R_{ld} and the datasets above, with r^2 ranging from 0.87 to 0.98 across the datasets for clear-sky and all-sky conditions. We then used the equations to show that changes in lower atmospheric heat storage explain more than 95% and around 73% of diurnal range and seasonal variations in R_{ld}, respectively, with the regional contribution decreasing with latitude. Seasonal changes in the emissivity of the atmosphere play a second role, which is controlled by anomalies in cloud cover at high latitudes but dominated by water vapor changes at mid-latitudes and subtropics, especially over monsoon regions. We also found that as aridity increases over the region, the contributions from changes in emissivity and lower atmospheric heat storage tend to offset each other (-40 W m^{-2} and 20-30 W m^{-2}, respectively), explaining the relatively small decrease in R_{ld} with aridity (-(10-20) W/m^{-2}). These equations thus provide a solid physical basis for understanding the spatiotemporal variability of surface downwelling longwave radiation. This should help to better understand and interpret climatological changes, such as those associated with extreme events and global warming.

1 Introduction

In the global mean surface energy budget, downward longwave radiation (R_{ld}) is dominant surface energy input (333 W/m^2 in global mean and 306 W^2/m over land), contributing around twice as much energy as absorbed solar radiation (161 W/m^2 in global mean and 184 W^2/m over land) (Trenberth et al. 2009, Wild et al. 2015). This dominance holds over all regions in the climatological mean, although there are some clear variations in space and time (Figs. 1 and S1). It is central to global warming, reflecting the greenhouse effect of the atmosphere (Held and Soden 2000), and its variations have been suggested to be the main contributor to some regional warming amplifications, such as in the Arctic (Lee et al. 2017) and the Tibetan Plateau (Su et al. 2017). Therefore, it is important to understand the main sources of variations in this surface energy balance term, which can be seen in Figure 1.

The flux of downwelling longwave radiation is influenced by the radiative properties of the entire atmospheric column, i.e., water vapour, clouds, and greenhouse gases, but also by the heat stored in the atmosphere, i.e., the temperature at which radiation is emitted back to the surface. To obtain an estimate of this flux, Brutsaert (1975) used functional expressions for the typical temperature and humidity profiles of the lower troposphere together with radiative transfer equations and semiempirical relationships of the absorptivity by water vapor, integrated these vertically, and expressed the resulting flux R_{ld} in terms of near-surface air temperature and water vapour pressure for clear-sky conditions. He thereby derived a semi-empirical equation for R_{ld} for an effective clear sky emissivity (ε_{cs}) and the corresponding flux of downwelling longwave radiation ($R_{ld,cs}$):

$$\varepsilon_{cs} = 1.24(e_a/T_a)^{1/7}, \tag{1}$$

$$R_{ld,cs} = \varepsilon_{cs}\sigma {T_a}^4. \tag{2}$$

where σ is Stefan–Boltzmann constant (σ = 5.67 10^{-8} W m^{-2} K^{-4}), e_a is the 2m water vapor pressure (unit: millibars) and T_a is the 2m air temperature (unit: K). The latter two meteorological variables can easily be obtained or inferred from weather stations, so that the downwelling flux of longwave radiation can be estimated from weather station observations. Note that the ε_{cs} shown in equation 1 is largely insensitive to changes in T_a. As a result, emissivity does not have a direct dependence on T_a, except that higher temperature may also lead to higher values in e_a.

This equation was later extended to all-sky conditions that include the effects of cloud cover, among which Crawford and Duchon (1999) is a common extension (Alados et al. 2012; Duarte et al. 2006; Flerchinger et al. 2009). This extension diagnoses cloud cover fraction (f_c) as the fraction of incoming solar radiation at the surface (R_s) in relation to the potential solar radiation ($R_{s,pot}$), that is, the incoming flux at the top of the atmosphere. The emissivity for all-sky conditions, ε, is then calculated as the mix of the emissivities of clear-sky conditions (Eqn. (1), weighted by the cloud-free proportion, $(1 - f_c)$ and clouds with an emissivity of $\varepsilon_c = 1$ (weighted by the cloud fraction f_c). Using this emissivity, the estimation of downwelling longwave radiation is then done by

$$f_c = 1 - R_s/R_{s,pot}, \tag{3}$$

$$\varepsilon = f_c + (1 - f_c)\varepsilon_{cs}, \tag{4}$$

$$R_{ld} = \varepsilon\sigma {T_a}^4. \tag{5}$$

Previous studies have already verified Equations 4-5 to have a very good agreement with site measurements with the r^2 of 0.883 and RMSE of 15.367 W/m^2 (Duarte et al. 2006; Hatfield et al. 1983), especially when the temperature is higher than 0℃ (Aase and Idso 1978; Satterlund 1979). Other studies have worked to calibrate and modify this estimate further to different regions (Malek 1997; Sridhar and Elliott 2002).

This expression for downwelling longwave radiation R_{ld} given by Eqn. (5) allows us to quantify the different contributions by cloud cover, f_c, water vapor concentrations, e_a (as a measure of the total water vapor content of the atmospheric column), and air temperature, T_a (as a proxy for the heat storage within the lower atmosphere, Panwar et al. 2022). With this, we can then attribute variations in R_{ld} to their physical causes.

Here, our aim is to first evaluate this estimate for downwelling longwave radiation with current global datasets at the continental scale. These variations are illustrated using the NASA-CERES (EBAF 4.1) dataset (Loeb et al., 2018; Kato et al., 2018, NASA/LARC/SD/ASDC 2017) and the NASA-CERES Syn1deg dataset (Doelling et al., 2013, 2016) in Figure 1 and are compared to variations in solar radiation. It can be seen that the climatological distribution of R_{ld} is mostly associated with latitudes, while also presenting some zonal variations, e.g., across western and eastern North America. In comparison, the seasonal cycle of R_{ld} is less determined by latitudes (Fig. 1b). It has a larger magnitude over land than over oceans, over arid regions than humid regions, and over cold regions more than over warm ones. Although studies have revealed a close correlation between the variation of R_{ld} and other factors like air temperature, water vapor, and CO_2 concentration (Wang and Liang 2009; Wei et al. 2021), here we go beyond correlations and rather attribute these variations to the different terms in Eqns. (1)-(5) that represent different radiative properties affecting R_{ld}.

To figure out the dominant driver for these spatiotemporal variations, we decompose changes in R_{ld} into its components: cloud cover, f_c, heat storage changes of atmosphere as reflected by 2m air temperature, T_a, and air humidity, e_a, by performing the differentiation of these equations. We show that heat storage changes predominantly shape the diurnal range and seasonal cycle of R_{ld}, while cloud cover variations play a second role in most cases. In addition, the temporal variations of R_{ld} are less over the ocean than over land, and less during winter than summer. On the other hand, the spatial variations of R_{ld} from arid to humid regions is relatively small, which we will show is due to a compensating effect of corresponding changes in atmospheric emissivity and heat storage.

Our paper is organized as follows: After briefly describing the datasets used in our evaluation in Section 2, we first the estimate of R_{ld} from these equations at the global scale, using multiple datasets in Section 3.1. After showing that the annual-mean and large-scale variations are well captured, we then use the equations to decompose the temporal variations of R_{ld} in terms of its mean spatial and temporal variations and relate these to their causes in Section 3.2. The spatial variations of R_{ld} are then further discussed in Section 3.3 in terms of its relationship with aridity. We then close with a brief summary and broader implications.

2 Datasets

To test R_{ld} estimates, we use FLUXNET half-hour observations (Pastorello et al. 2020, half-hourly values, 189 sites, see Table S1 and Figure S2 for details), the NASA-CERES monthly satellite-based radiation dataset (Doelling et al., 2013, 2016, monthly means, covering years 2001 to 2018), and the ERA5 monthly reanalysis dataset (Hersbach et al. 2018, monthly means, covering years 1979 to 2021).

For each dataset, T_a, e_a, and f_c are needed as inputs for Eqs. (1)-(5), while R_{ld} data is used for the comparison. Cloud cover f_c is calculated using Eq. (3) for all three datasets with incoming solar radiation at the surface (R_s) and the potential solar radiation ($R_{s,pot}$). For NASA-CERES estimation, T_a from the CPC Global Unified Temperature dataset (CPC Global Unified Temperature) is used as temperature observation.

For all three datasets, water vapor pressure, e_a, is not directly given. It is calculated from the water vapor deficit (VPD, FLUXNET) or dewpoint temperature (T_{dew}, ERA5) using Monteith and Unsworth (2008):

$$e_a = 6.1079 \times \exp\,(17.269 T_{dew}/(237.3 + T_{dew})), \tag{6}$$

$$e_a = 6.1079 \times \exp\,(17.269 T_a/(237.3 + T_a)) - VPD, \tag{7}$$

And the calculated e_a from ERA5 is also used in NASA-CERES estimation.

For the analysis of the spatial variations of R_{ld} along water availability, we use the aridity index ($\mathrm{AI} = \frac{R}{LP}$) (Budyko 1958; UNCOD 1977). This index is calculated using the mean annual net radiation (R) taken from the NASA-CERES dataset, the mean annual net precipitation (P) taken from the CPC Global Unified Gauge-Based Analysis of Daily Precipitation data (Chen et al. 2008 and Xie et al. 2007, CPC Global Unified Gauge-Based Analysis of Daily Precipitation), and a latent heat of vaporization for water of $L = 2260$ kJ/kg. A larger value of AI indicates stronger aridity.

3 Results and discussion

3.1 Comparison to observed, satellite, and reanalysis data

We first compared the estimates of R_{ld} at a point-by-point basis separately for clear-sky and all-sky conditions using Eqns. (2) and (5), respectively. This comparison is shown in Figure 2 using FLUXNET, CERES, and ERA5 data. The estimates correlate very well with r^2 of 0.92 and 0.87 for clear-sky and all-sky conditions, respectively, and RMSE values of 18.24 and 24.56 W m^{-2}. The slope of the linear regressions between the estimated and observed R_{ld} for FLUXNET are 1.03 and 1.02, with most data points being concentrated around the 1:1 line (Figs. 2a and 2b). Note that for all-sky conditions, the agreement is slighty less good, with a lower correlation coefficient and a larger RSME. The agreement with the NASA-CERES and ERA5 datasets are even better, with higher correlation coefficients and lower RSME.

Despite this high level of agreement of the estimates, we can see some systematic biases in the estimates for R_{ld}. These can be seen in Figure 3 and Figure S3, which show the spatial distribution of these biases and their variations against temperature and humidity. For clear-sky conditions, there appears to be a general underestimation in the high latitudes and, to some extent, in arid regions (Figs. 3c and 3e). Brutsaert (1975) already described that for very low temperatures and in arid conditions, there are better parameter values than those used in Eq. 1, with a larger coefficient than 1.24 and a different exponent. This can then lead to an underestimation of Rld under low humidity (Figs. 3a, S3a, S3c). Moreover, B75 has not considered the gradual increase in emissivity as temperature decreases below freezing (Aase and Idso 1978), thus explaining the underestimation under low temperature (Figs. 3b, S3b, S3b). The biases seen in Figure 3 are nevertheless notably smaller than the spatial-temporal variations shown in Figure 1. This means that these biases do not prevent us from using Brutsaert to attribute the causes for the seasonal variation and the spatial range of R_{ld}.

The biases for all-sky conditions generally share the distribution with that of clear-sky conditions, with a smaller magnitude (Figs. 3b, 3d and 3f), which are also small compared to the spatial-temporal variations.

Overall, this evaluation shows that the expressions given by Eqns. (1) - (5) are very well suited to describe the spatiotemporal variations of R_{ld} for current climatological conditions.

3.2 Attribution of diurnal and seasonal variations

We next use Eqns. (1) - (5) to attribute temporal variations of R_{ld} to their physical causes. To do so, we can express changes ΔR_{ld} as a function of changes in water vapor, Δe_a, cloud cover, Δf_c, and air temperature, ΔT_a. The functional dependence is derived from the equations by differentiation and applying the chain rule. In a first step, we express a change ΔR_{ld} by the partial contributions $\Delta R_{ld,\varepsilon}$ and $\Delta R_{ld,T}$, that are due to changes in emissivity, $\Delta\varepsilon$, and due to changes in atmospheric heat storage that are associated with a change in air temperature ΔT_a:

$$\Delta R_{ld} = \Delta R_{ld,\varepsilon} + \Delta R_{ld,T} = \frac{\partial R_{l,d}}{\partial \varepsilon}\Delta\varepsilon + \frac{\partial R_{l,d}}{\partial T_a}\Delta T_a = \sigma\overline{T_a}^4\Delta\varepsilon + 4\sigma\bar{\varepsilon}\overline{T_a}^3\Delta T_a. \quad (8)$$

The 2 terms at the right side of Eq. 8 are $\Delta R_{ld,\varepsilon}$ and $\Delta R_{ld,T}$, respectively.

The contribution $\Delta R_{ld,\varepsilon}$ is further decomposed into contributions $\Delta R_{ld,f_c}$, $\Delta R_{ld,e_a}$, and $\Delta R_{ld,T_a}{}'$ due to variations in clouds, Δf_c, air humidity, Δe_a, and surface temperature, ΔT_a. We obtain:

$$\Delta R_{ld,\varepsilon} = \sigma \overline{T_a}^4 \Delta\varepsilon \approx \sigma\overline{T_a}^4 \times \frac{\partial\varepsilon}{\partial f_c}\Delta f_c + \sigma\overline{T_a}^4 \times \frac{\partial\varepsilon}{\partial e_a}\Delta e_a + \sigma\overline{T_a}^4 \times \frac{\partial\varepsilon}{\partial T_a}\Delta T_a$$
$$= \sigma\overline{T_a}^4 \times \left(1 - 1.24\left(\frac{\overline{e_a}}{\overline{T_a}}\right)^{\frac{1}{7}}\right)\Delta f_c + \sigma\overline{T_a}^4 \times \frac{1.24}{7}\frac{\left(1-\overline{f_c}\right)}{(\overline{e_a})^{\frac{6}{7}}(\overline{T_a})^{\frac{1}{7}}}\Delta e_a \tag{9}$$
$$+ \sigma\overline{T_a}^4 \times \left(-\frac{1.24}{7}\right) \times \frac{\left(1-\overline{f_c}\right)(\overline{e_a})^{\frac{1}{7}}}{(\overline{T_a})^{\frac{8}{7}}} \times \Delta T_a) \,.$$

The 3 terms at the right side of Eq. 9 are $\Delta R_{ld,f_c}$, $\Delta R_{ld,e_a}$, and $\Delta R_{ld,T_a}{}'$, respectively.

Note that the third term is of less magnitude compared with the other two terms (e.g. in terms of the seasonal range as shown in Fig. 5f), which is hence not focused in this work.

We next applied this approach to the diurnal deviations ΔR_{ld} from the daily mean using the FLUXNET dataset. This decomposition is shown in Figure 4 in aggregated form across the FLUXNET sites for whole year (Fig. 4a), the Northern hemisphere summer (Fig. 4b) and winter seasons (Fig. 4c). More than 95% of the diurnal variations (of about ± 20 W m^{-2}) are caused by diurnal changes in air temperature, while variations in emissivity play practically no role (Fig. S4). Diurnal changes in air temperature reflect variations in heat storage of the atmospheric boundary layer. This is consistent with the notion that diurnal variations in solar radiation over land are buffered primarily by the lower atmosphere, rather than below the surface as it is the case for open water bodies and the ocean (Kleidon and Renner 2017). Since most of the stations in the FLUXNET dataset are located in the midlatitudes of the Northern hemisphere, the variations are consistently larger in summer due to the greater solar input (Fig. 4b) than in winter (Fig. 4c).

Figure 5 shows the same kind of decomposition, but for seasonal variations in R_{ld} in the NASA-CERES dataset, which is the difference between the maximum and minimum of monthly R_{ld} data. Generally, areas with relatively low annual-mean R_{ld}, e.g. the high latitude regions of North America and northeastern Eurasia, have the largest seasonal cycle (Fig. 1). The decomposition shows that this variation is mostly due to the seasonal variation in atmospheric heat storage ($\Delta R_{ld,T}$), with a portion of around 73% on a global scale, and the rest are attributed to the seasonal changes in water vapor (24%) and cloud cover (12%). Notably, seasonal variations in emissivity play a greater role than atmospheric heat storage in changing R_{ld} in tropical areas, especially over the monsoon region. This is predominantly due to the strong seasonal fluctuations in water vapor levels and cloud-cover (Figs. 5d-5f).

The aggregation to the global scale across land and ocean is shown in Fig. S5, where the deviations are calculated as the difference of the monthly means to the annual mean. Figs. S5 show that the seasonal variations of R_{ld} is generally less over the ocean than on the land, an effect that can also be seen in Fig. 1. The decomposition shows that these variations are mostly caused by changes in lower atmospheric heat storage, with a slight modulation by emissivity changes. This can, again, be largely explained by the effect described above for the diurnal variations (Kleidon and Renner 2017). Over the land, the changes in radiation are majorly buffered by the heat storage in the lower atmosphere by the variations in convective boundary layer height. However, over marine areas, solar radiation penetrates the transparent water bodies, the heat storage of which hence buffers the season cycle of the radiation over the ocean. Since the heat storage of the water body is larger than that of the lower atmospheric boundary layer, the buffering effect is consequently larger, which leads to the less seasonal cycle of the surface temperature and R_{ld} over the ocean.

In summary, what our decomposition shows is that most temporal variations in R_{ld} in current, climatological conditions are explained by heat storage changes within the lower atmosphere.

3.3 Attribution of geographic variations with aridity

Last, we applied the decomposition to the climatological variations in R_{ld} along with differences in mean water availability. Water availability was characterized by Budyko's aridity index (AI), with values AI < 1 representing humid regions, and larger values reflecting increased aridity. The spatial distribution of AI is shown in Fig. S6. Here, the deviations ΔR_{ld} are calculated with respect to the annual mean over land. The different contributions to the deviations are shown in Fig. 6, as well as the delineation along the aridity index (Figs. 6e - f).

The decomposition of the spatial distribution of the climatological means shows that the variations are largely caused by differences in lower atmospheric heat storage as well (Fig. 6a). The contribution due to variations in emissivity has a smaller magnitude (Fig. 6b), and is dominated by changes in cloud cover (Fig. 6c) and changes in water vapor (Fig. 6d) at high- and mid- latitudes respectively.

These variations are evaluated with respect to the aridity index in Figs. 6e, 6f and S7. While there is a large spread, as seen in the quantiles, there is a small, but consistent trend towards lower values of R_{ld} in more arid regions, with a magnitude of about -10~20 W m^{-2} across the entire aridity index spectrum (black dashed line in Figs. 6e and 6f). We also notice a shift in the contributions, with emissivity contributing less and lower atmospheric heat storage contributing more with increased values of AI. The decreasing contributions in emissivity of about -20~40 W m^{-2} is caused by reductions in cloud cover and water vapor (Figs. 6f), which can be attributed to the common presence of high-pressure systems in subtropical arid areas (Zampieri et al. 2009) and less monsoon there. The decreasing contribution by lower atmospheric emissivity is compensated for by an increased contribution of about +10~20 W m^{-2} by atmospheric heat storage that is caused by the generally warmer mean temperatures in arid regions.

4. Discussion and Conclusions

We found that the semiempirical equations of Brutsaert (1975) and Crawford and Duchon (1999) work very well to estimate the downwelling flux of longwave radiation by comparing these to estimates from observation, satellite, and reanalysis datasets, with r^2 ranging from 0.87 to 0.98 across the datasets for clear-sky and all-sky conditions. We then showed that one can use these equations to decompose this flux into different components, and relate changes to differences in cloud cover, water vapor, and lower atmospheric heat storage. We found that most diurnal changes in downwelling longwave radiation are caused by differences in lower atmospheric heat storage that are reflected in differences in surface air temperature, with the changes in atmospheric emissivity playing the secondary role. The dominance of surface air temperature can be also observed in the seasonal ranges of R_{ld}, except in tropical monsoon regions due to large variations in water vapor and cloud-cover. As for the spatial variation, from arid to humid region, the increasing lower atmospheric heat storage and decreasing atmospheric emissivity have an offsetting effect on the R_{ld} variation, thus leading to relatively subtle changes in Rld along with aridity index.

Relating our decomposition to radiative kernel helps to gain a more comprehensive understanding of variations in R_{ld}. Referring to the sensitivity in the downwelling longwave radiation for an incremental change in an atmospheric property (e.g., T_a, f_c, and e_a), radiative kernel has been used to attribute R_{ld} changes, based on numerically calculation with radiative transfer code (Previdi 2010 and Vargas Zeppetello et al. 2019) or partial differentiating with explicit formula for R_{ld} (Shakespeare and Roderick, 2022). Following Shakespeare and Roderick (2022), the approximate radiative kernel of T_a, f_c, and e_a are calculated based on Eqs. 8-9 (i.e., $\frac{\partial R_{ld}}{\partial T} = 4\sigma\bar{\varepsilon}\overline{T_a}^3$, $\frac{\partial R_{ld}}{\partial f_c} = \sigma\overline{T_a}^4 \times \left(1 - 1.24\left(\frac{\overline{e_a}}{\overline{T_a}}\right)^{\frac{1}{7}}\right)$, and $\frac{\partial R_{ld}}{\partial e_a} = \sigma\overline{T_a}^4 \times \frac{1.24}{7}\frac{(1-\overline{f_c})}{(\overline{e_a})^{\frac{6}{7}}(\overline{T_a})^{\frac{1}{7}}}$) and shown in the left panel of Fig. S8. As shown in Fig S8a, the sensitivity of R_{ld} to T_a peaks in the tropics with a maximum of around 5 W/m^2/K and decreases at higher latitudes, which is generally consistent with Shakespeare & Roderick (2022). Moreover, the seasonal cycle of the atmospheric properties themselves are shown in the right panel of Figure S8, which reveals that the spatial distribution of the contribution of

T_a, e_a, and f_c to the seasonal variations in R_{ld} (Figure 5) is dominated by the seasonal changes of the air properties (Figs. S8b, S8d, and S8f) instead of the sensitivity of R_{ld} to them (Figs. S8a, S8c, and S8e).

These equations can then be applied to different aspects of climate research. For instance, the values of downwelling longwave radiation are often missing in FLUXNET data (Table S2), and these equations can be used to fill the gaps with air temperature and humidity observations. We can also use these equations to better understand the physical mechanisms for temperature change due to extreme events. For instance, Park et al. (2015) and Alekseev et al. (2019) found that an enhancement of downwelling longwave radiation in the Arctic is found to be preceded by the advection of moisture and heat. The equations by Brutsaert (1975) and Crawford and Duchon (1999) can then be used to quantify the individual contributions by the advection of heat and moisture (Tian et al. 2022). Another example is the attribution of differences in temperature magnitudes across humid and arid regions (Ghausi et al., 2023). Du et al. (2020) used these equations to explain why global warming was stronger during clear-sky conditions in observations in China due to the greater sensitivity of clear-sky emissivity to a change in water vapor. This was then used to explain the observed, stronger global warming in the arid regions of China, which have less clouds and a higher frequency of clear-sky conditions than the humid regions. Furthermore, while the empirical coefficient of 1.24 in Eq. (1) may change due to emissivity changes from greenhouse gases, this formulation can nevertheless provide a useful basis in terms of the interannual changes of R_{ld}, which is shown in Fig. S9. As shown in Fig. S9a, R_{ld} increases in most of the land regions, at an average rate of 0.64 W/m^2/decade, with the contribution of increased temperature, increased water vapor, and decreased cloud cover contributing 0.46, 0.28, -0.10 W/m^2/decade, respectively. Furthermore, it can be observed in Figs. S9d-S9i that the temperature effect is generally around 0.5 W/m^2/decade, while the influence of emissivity is significantly dominant in the monsoon region, which is majorly due to the interannual changes in water vapor.

It is worth noting that several effects on Rld variations are not included in B75 and C&D99, e.g., the well-mixed greenhouse gas concentrations (Shakespeare and Roderick, 2022), large aerosol particles (Zhou and Savijärvi. 2013), and cloud base (Viúdez-Mora et al. 2015). Although rarely influencing the diurnal change, seasonal cycles, and spatial distribution, these terms needs attention when the interannual trend of Rld is investigated under global warming, which can be implied by the difference between Figs. S9a and S9b. In addition, B75 in conjunction with C&D99 is adopted in this work to decompose the Rld variations in different spatial-temporal scales, considering its solid physical foundations and the relatively less computation consumption. Further analysis can be performed based on other estimations, e.g. Prata 1996, which shows consistency with reanalysis data (Allan et al. 2004). The cloud effect can be also detected using the difference between all-sky and clear-sky Rld (Allan 201; Ghausi et al., 2022). Moreover, datasets that are more focused on radiation and energy budget can be used to test the robust of the results, e.g., BSRN (Driemel et al. 2018) and GEBA (Wild et al. 2017).

We conclude that the equations by Brutsaert (1975) and Crawford and Duchon (1999) are still very useful in advancing our understanding of surface temperature changes. Our evaluation has shown how well these equations estimate this flux, and our application to the decomposition of different contributions has shown its utility in understanding the causes of its variation. These equations should help us to better understand aspects of climate variability, extreme events, and global warming, linking these to the mechanistic contributions by downwelling longwave radiation.

Acknowledgments

This research is supported by the National Natural Science Foundation of China (52209026) and the Second Tibetan Plateau Scientific Expedition and Research Program (grant no. 2019QZKK0208). This research resulted from a research stay of YLT in AK's research group. This stay was supported by China Scholarship

Council as No. 202106210161. AK and SAG acknowledge funding from the Volkswagen Stiftung through the ViTamins project.

Author contributions

YLT, SAG, and AK conceived and designed the analysis, with inputs from DZ and GW. YLT performed the analysis and discussed the results with all authors. YLT and AK wrote the paper.

Competing interests

The contact author has declared that none of the authors has any competing interests.

Data availability

The data used in this study was downloaded from the links provided with the references. No new data was created.

References

Aase, J. K., and S. B. Idso, 1978: A comparison of two formula types for calculating long-wave radiation from the atmosphere. Water Resources Research, 14, 623-625. https://doi.org/10.1029/WR014i004p00623

Alados, I., I. Foyo-Moreno, and L. Alados-Arboledas, 2012: Estimation of downwelling longwave irradiance under all-sky conditions. International Journal of Climatology, 32, 781-793. https://doi.org/10.1002/joc.2307

Allan, R. P., Ringer, M. A., Pamment, J. A., and Slingo, A. (2004), Simulation of the Earth's radiation budget by the European Centre for Medium-Range Weather Forecasts 40-year reanalysis (ERA40), J. Geophys. Res., 109, D18107, https://doi.org/10.1029/2004JD004816 .

Alekseev, G., S. Kuzmina, L. Bobylev, A. Urazgildeeva, and N. Gnatiuk, 2019: Impact of atmospheric heat and moisture transport on the Arctic warming. Int. J. Climatol., 39, 3582–3592, https://doi.org/10.1002/joc.6040.

Budyko, M. I. (1958) The Heat Balance of the Earth's Surface, trs. Nina A. Stepanova, US Department of Commerce, Washington, D.D., 259 p.

Brutsaert, W., 1975: On a derivable formula for long-wave radiation from clear skies. Water Resources Research, 11, 742-744. https://doi.org/10.1029/WR011i005p00742 .

Crawford, T. M., and C. E. Duchon, 1999: An Improved Parameterization for Estimating Effective Atmospheric Emissivity for Use in Calculating Daytime Downwelling Longwave Radiation. Journal of Applied Meteorology, 38, 474-480. https://doi.org/10.1175/1520-0450(1999)038<0474:Aipfee>2.0.Co;2

Chen, M., W. Shi, P. Xie, V. B. S. Silva, V E. Kousky, R. Wayne Higgins, and J. E. Janowiak (2008), Assessing objective techniques for gauge-based analyses of global daily precipitation, J. Geophys. Res., 113, D04110, >), https://doi.org/10.1029/2007JD009132.

CPC Global Unified Temperature. Available online: https://psl.noaa.gov/data/gridded/data.cpc.globaltemp.html, provided by the NOAA PSL, Boulder, Colorado, USA, from their website at https://psl.noaa.gov (accessed on 6 March 2022).

CPC Global Unified Gauge-Based Analysis of Daily Precipitation. Available online: https://psl.noaa.gov/data/gridded/data.cpc.globalprecip.html, provided by the NOAA PSL, Boulder, Colorado, USA, from their website at https://psl.noaa.gov (accessed on 5 March 2022)

Driemel, A., Augustine, J., Behrens, K., Colle, S., et al. (2018) Baseline Surface Radiation Network (BSRN): structure and data description (1992–2017), Earth Syst. Sci. Data, 10, 1491–1501, https://doi.org/10.5194/essd-10-1491-2018 .

Du, M., Kleidon, A., Sun, F., Renner, M., & Liu, W. (2020). Stronger global warming on nonrainy days in observations from China. Journal of Geophysical Research: Atmospheres, 125, e2019JD031792. https://doi.org/10.1029/2019JD031792

Doelling, D. R., Loeb, N. G., Keyes, D. F., Nordeen, M. L., Morstad, D., Nguyen, C., and Sun, M.: Geostationary enhanced temporal interpolation for CERES flux products, J. Atmos. Ocean. Tech., 30, 1072–1090, 2013. https://doi.org/10.1175/JTECH-D-12-00136.1

Doelling, D. R., Sun, M., Nguyen, L. T., Nordeen, M. L., Haney, C. O., Keyes, D. F., and Mlynczak, P. E.: Advances in geostationary-derived longwave fluxes for the CERES synoptic (SYN1 deg) product, J. Atmos. Ocean. Tech., 33, 503–521, 2016. https://doi.org/10.1175/JTECH-D-15-0147.1

Duarte, H. F., N. L. Dias, and S. R. Maggiotto, 2006: Assessing daytime downward longwave radiation estimates for clear and cloudy skies in Southern Brazil. *Agricultural and Forest Meteorology*, **139,** 171-181. https://doi.org/10.1016/j.agrformet.2006.06.008

Flerchinger, G. N., W. Xaio, D. Marks, T. J. Sauer, and Q. Yu, 2009: Comparison of algorithms for incoming atmospheric long-wave radiation. *Water Resources Research*, **45**. https://doi.org/10.1029/2008WR007394

Ghausi, S. A., Tian Y., Zehe E., & Kleidon A. (2023) Radiative controls by clouds and thermodynamics shape surface temperatures and turbulent fluxes over land. Proceedings of the National Academy of Sciences. 120 (29), e2220400120. https://doi.org/10.1073/pnas.2220400120

Ghausi, S. A., Ghosh, S., & Kleidon, A. (2022). Breakdown in precipitation–temperature scaling over India predominantly explained by cloud-driven cooling. *Hydrology and Earth System Sciences*, *26*(16), 4431-4446. https://doi.org/10.5194/hess-26-4431-2022

Hatfield, J. L., R. J. Reginato, and S. B. Idso, 1983: Comparison of long-wave radiation calculation methods over the United States. *Water Resources Research*, **19,** 285-288. https://doi.org/10.1029/WR019i001p00285

Held, I. M., and B. J. Soden, 2000: Water Vapor Feedback and Global Warming. Annual Review of Energy and the Environment, 25, 441-475. https://doi.org/10.1146/annurev.energy.25.1.441

Hersbach, H., and Coauthors, 2018: ERA5 hourly data on single levels from 1959 to present. Copernicus Climate Change Service (C3S) Climate Data Store (CDS). (Accessed on < 06-03-2022 >), https://doi.org/10.24381/cds.adbb2d47 .

Kato, S., Rose, F. G., Rutan, D. A., Thorsen, T. E., Loeb, N. G., Doelling, D. R., Huang, X., Smith, W. L., Su, W., and Ham, S.-H.: Surface irradiances of Edition 4.0 Clouds and the Earth's Radiant Energy System (CERES) Energy Balanced and Filled (EBAF) data product, J. Climate, 31, 4501–4527, https://doi.org/10.1175/JCLI-D-17-0523.1, 2018.

Kleidon, A., and M. Renner, 2017: An explanation for the different climate sensitivities of land and ocean surfaces based on the diurnal cycle. Earth Syst. Dynam., 8, 849-864. https://doi.org/10.5194/esd-8-849-2017

Lee, S., T. Gong, S. B. Feldstein, J. A. Screen, and I. Simmonds, 2017: Revisiting the Cause of the 1989–2009 Arctic Surface Warming Using the Surface Energy Budget: Downward Infrared Radiation Dominates the Surface Fluxes. Geophysical Research Letters, 44, 10,654-610,661. https://doi.org/10.1002/2017GL075375.

Loeb, N. G., Doelling, D. R., Wang, H., Su, W., Nguyen, C., Corbett, J. G., Liang, L., Mitrescu, C., Rose, F. G., and Kato, S.: Clouds and the Earth's Radiant Energy System (CERES) Energy Balanced and Filled (EBAF) Top-of-Atmosphere (TOA) Edition-4.0 data product, J. Climate, 31, 895–918, https://doi.org/10.1175/JCLI-D-17-0208.1, 2018.

Esmael Malek, 1997. Evaluation of effective atmospheric emissivity and parameterization of cloud at local scale. Atmospheric Research, 45 (1), 41-54, https://doi.org/10.1016/S0169-8095(97)00020-3 .

Monteith, J.L. and Unsworth, M.H. (2008) Principles of Environmental Physics. 3rd Edition, Academic Press, New York, 418. https://doi.org/10.1016/C2010-0-66393-0

NASA/LARC/SD/ASDC. (2017). CERES and GEO-Enhanced TOA, Within-Atmosphere and Surface Fluxes, Clouds and Aerosols Monthly Terra-Aqua Edition4A [Data set]. NASA Langley Atmospheric Science Data Center DAAC. (Accessed on < 09-03-2022 >), https://doi.org/10.5067/TERRA+AQUA/CERES/SYN1DEGMONTH_L3.004A.

Panwar, A., and A. Kleidon, 2022: Evaluating the Response of Diurnal Variations in Surface and Air Temperature to Evaporative Conditions across Vegetation Types in FLUXNET and ERA5. J. Climate, 35, 6301–6328, https://doi.org/10.1175/JCLI-D-21-0345.1.

Park, H.-S., S. Lee, S.-W. Son, S. B. Feldstein, and Y. Kosaka, 2015: The impact of poleward moisture and sensible heat flux on Arctic winter sea ice variability. J. Climate, 28, 5030–5040, https://doi.org/10.1175/JCLI-D-15-0074.1

Pastorello, G., and Coauthors, 2020: The FLUXNET2015 dataset and the ONEFlux processing pipeline for eddy covariance data. Scientific Data, 7, 225. https://doi.org/10.1038/s41597-020-0534-3

Prata, A.J. (1996), A new long-wave formula for estimating downward clear-sky radiation at the surface. Q.J.R. Meteorol. Soc., 122: 1127-1151. https://doi.org/10.1002/qj.49712253306

Previdi, M. (2010). Radiative feedbacks on global precipitation. Enviromental Research Letters, 5, 025211. https://doi.org/10.1088/1748-9326/5/2/025211

Sridhar V, Ronald L Elliott, 2022: On the development of a simple downwelling longwave radiation scheme, Agricultural and Forest Meteorology, 112, 3–4, 237-243, https://doi.org/10.1016/S0168-1923(02)00129-6.

Satterlund, D. R., 1979: An improved equation for estimating long-wave radiation from the atmosphere. Water Resources Research, 15, 1649-1650. https://doi.org/10.1029/WR015i006p01649

Shakespeare C. J. and M. Roderick. (2022). Diagnosing Instantaneous Forcing and Feedbacks of Downwelling Longwave Radiation at the Surface: A Simple Methodology and Its Application to CMIP5 Models. Journal of Climate. https://doi.org/10.1175/JCLI-D-21-0865.1

Su, J., A. Duan, and H. Xu, 2017: Quantitative analysis of surface warming amplification over the Tibetan Plateau after the late 1990s using surface energy balance equation. Atmospheric Science Letters, 18, 112-117. https://doi.org/10.1002/asl.732

Tian, Y., Zhang, Y., Zhong, D., Zhang, M., Li, T., Xie, D., & Wang, G. (2022). Atmospheric Energy Sources for Winter Sea Ice Variability over the North Barents–Kara Seas, Journal of Climate, 35(16), 5379-5398. https://doi.org/10.1175/JCLI-D-21-0652.1

Trenberth, K. E., Fasullo, J. T., & Kiehl, J. (2009). Earth's Global Energy Budget, *Bulletin of the American Meteorological Society*, *90*(3), 311-324. https://doi.org/10.1175/2008BAMS2634.1

Vargas Zeppetello, L. R., Donohoe, A., & Battisti, D. S. (2019). Does surface temperature respond to or determine downwelling longwave radiation? Geophysical Research Letters, 46, 2781–2789. https://doi.org/10.1029/2019GL082220

Viúdez-Mora, A., Costa-Surós, M., Calbó, J., and González, J. A. (2015), Modeling atmospheric longwave radiation at the surface during overcast skies: The role of cloud base height, J. Geophys. Res. Atmos., 120, 199–214, https://doi.org/10.1002/2014JD022310

Wang, K., and S. Liang, 2009: Global atmospheric downward longwave radiation over land surface under all-sky conditions from 1973 to 2008. *Journal of Geophysical Research: Atmospheres*, **114**. https://doi.org/10.1029/2009JD011800

Wei, Y., and Coauthors, 2021: Trends and Variability of Atmospheric Downward Longwave Radiation Over China From 1958 to 2015. *Earth and Space Science*, **8,** e2020EA001370. https://doi.org/10.1029/2020EA001370

Wild, M., Folini, D., Hakuba, M.Z. et al. The energy balance over land and oceans: an assessment based on direct observations and CMIP5 climate models. Clim Dyn 44, 3393–3429 (2015). https://doi.org/10.1007/s00382-014-2430-z

Wild, M., Ohmura, A., Schär, C., Müller, G., Folini, D., Schwarz, M., Hakuba, M. Z., and Sanchez-Lorenzo, A.: The Global Energy Balance Archive (GEBA) version 2017: a database for worldwide measured surface energy fluxes, Earth Syst. Sci. Data, 9, 601–613, https://doi.org/10.5194/essd-9-601-2017, 2017.

Xie, P., Chen, M., Yang, S., Yatagai, A., Hayasaka, T., Fukushima, Y., & Liu, C. (2007). A Gauge-Based Analysis of Daily Precipitation over East Asia, Journal of Hydrometeorology, 8(3), 607-626. https://doi.org/10.1175/JHM583.1.

Zampieri, M., F. D'Andrea, R. Vautard, P. Ciais, N. de Noblet-Ducoudré, and P. Yiou, 2009: Hot European Summers and the Role of Soil Moisture in the Propagation of Mediterranean Drought. *Journal of Climate*, **22,** 4747-4758. https://doi.org/10.1175/2009JCLI2568.1

Zhou and Savijärvi. 2014. The effect of aerosols on long wave radiation and global warming. Atmospheric Research, 135–136: 102-111 https://doi.org/10.1016/j.atmosres.2013.08.009

Figures

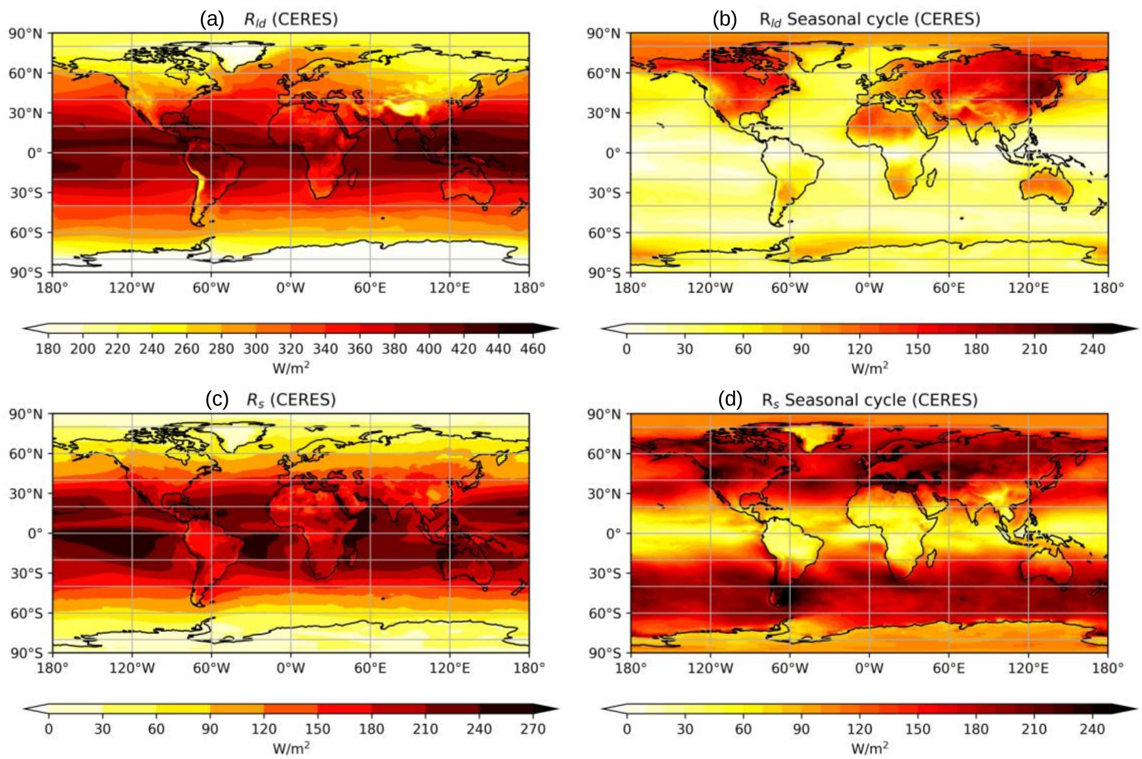

Figure 1. Spatial distribution of (a, c) the climatological mean and (b, d) the seasonal amplitude of downward longwave radiation and absorbed solar radiation at the surface respectively from the NASA-CERES dataset. The seasonal amplitude is calculated as the difference between the maximum and minimum monthly data.

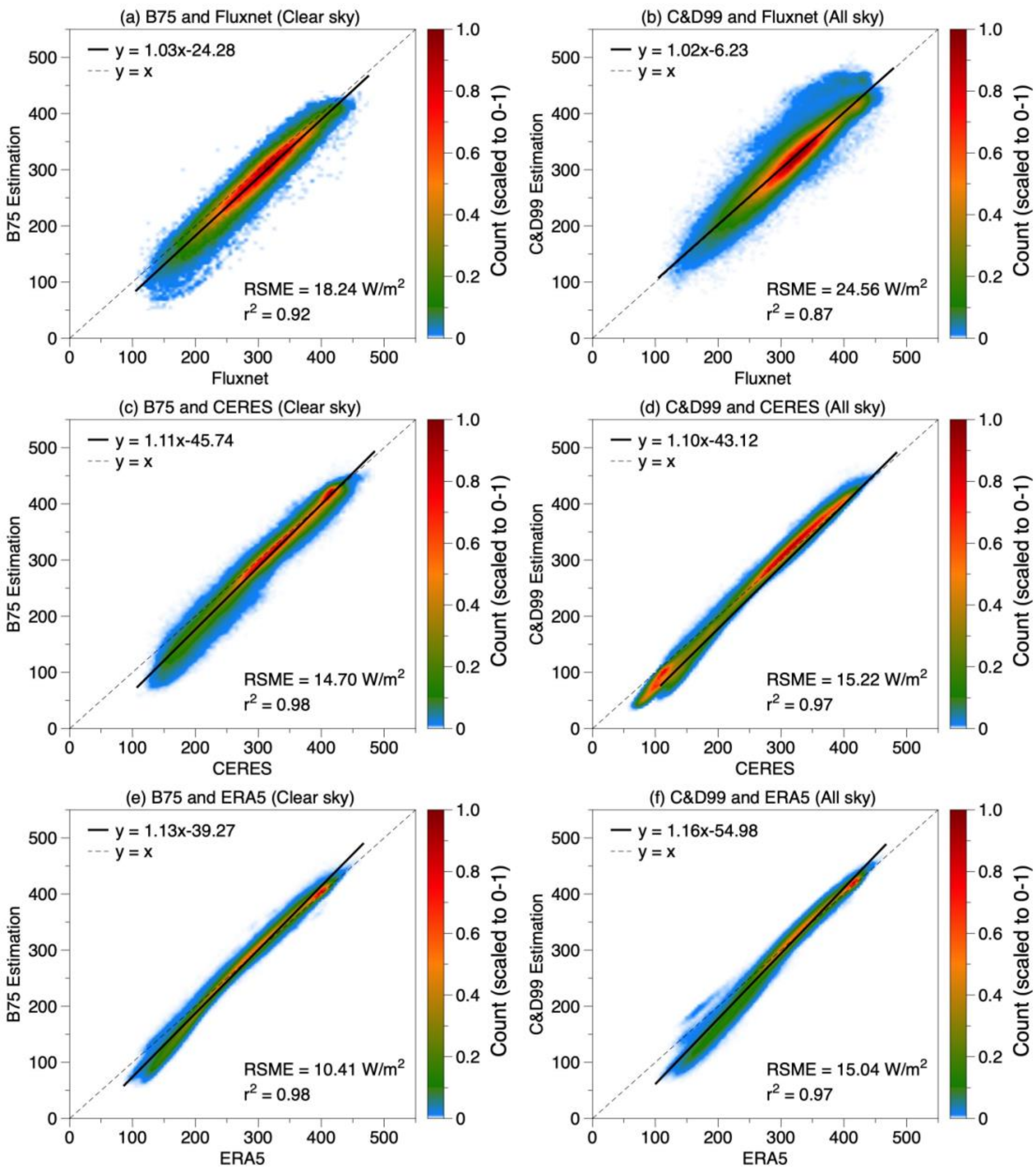

Figure 2. Comparison of Rld estimated by Brutsaert (1975) (a, c, e) for clear-sky conditions and by Crawford and Duchon (1999) (b, d, f) for all-sky conditions using (a, b) FLUXNET hourly data of 189 sites, (c, d) NASA-CERES monthly data of 1°×1° from 2001 to 2018 and (e, f) ERA5 monthly data of resolution of 1°×1° from 1979 to 2021. Colors indicate the density of the data points and is scaled to values between 0 - 1.

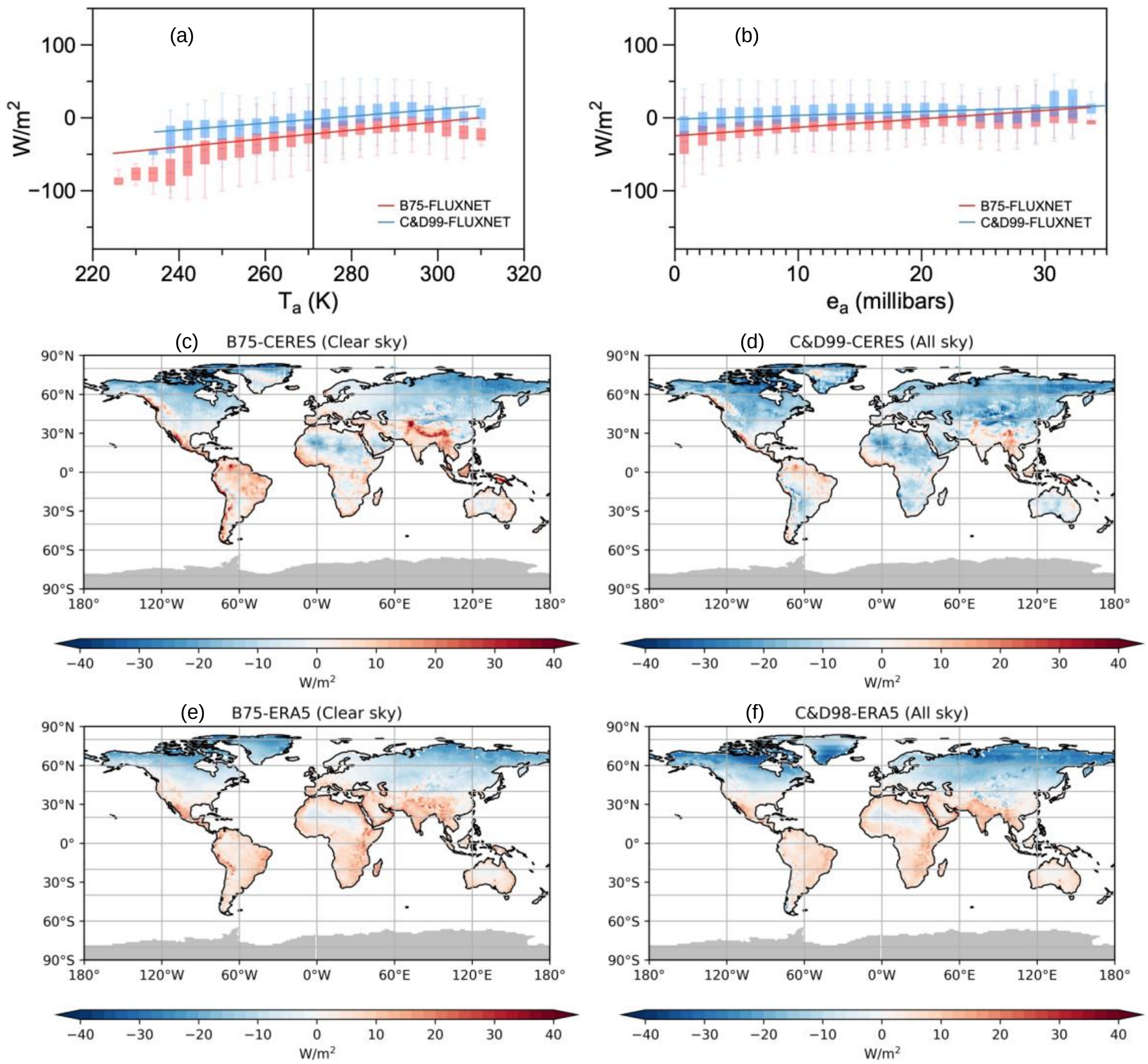

Figure 3. Biases in the estimates for multi-year mean R_{ld} for FLUXNET data of 189 sites against (a) air temperature and (b) water vapor pressure. Distribution of biases in the estimates for multi-year mean R_{ld} for (c, d) NASA-CERES data from 2001 to 2018 and (e, f) ERA reanalysis from 1979 to 2021 for (c, e) clear-sky and (d, f) all-sky conditions over land. Grey shading indicates missing values.

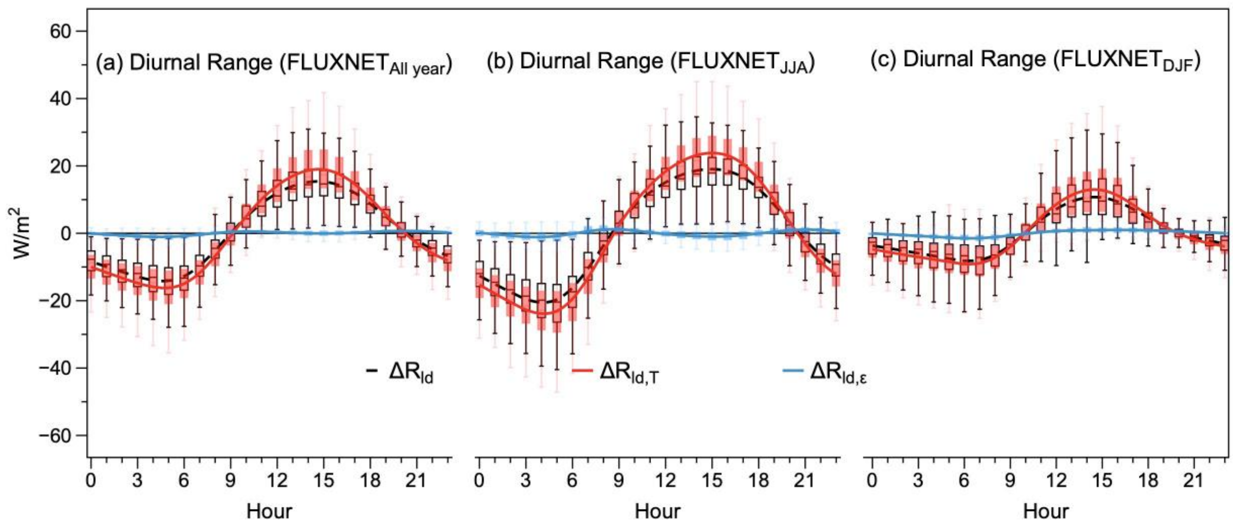

Figure 4. The multi-year average diurnal variations in R_{ld} (black dashed line) and its decomposition into contributions by changes in emissivity (blue, $\Delta R_{ld,\varepsilon}$) and lower atmospheric heat storage (red, $\Delta R_{ld,T}$) in the FLUXNET dataset aggregated over 189 sites for (a) the whole year, (b) June-August, and (c) December – February. The box shows the variation among the 189 sites. The upper and lower whiskers indicate 95th and 5th percentiles, upper boundary, median line, and lower boundary of the box indicate the 75th, 50th, and 25th quantiles, respectively. For each site and each day, the daily mean value is removed, with the deviations shown. Regression lines are based on site-mean or grid-mean value using LOESS regression.

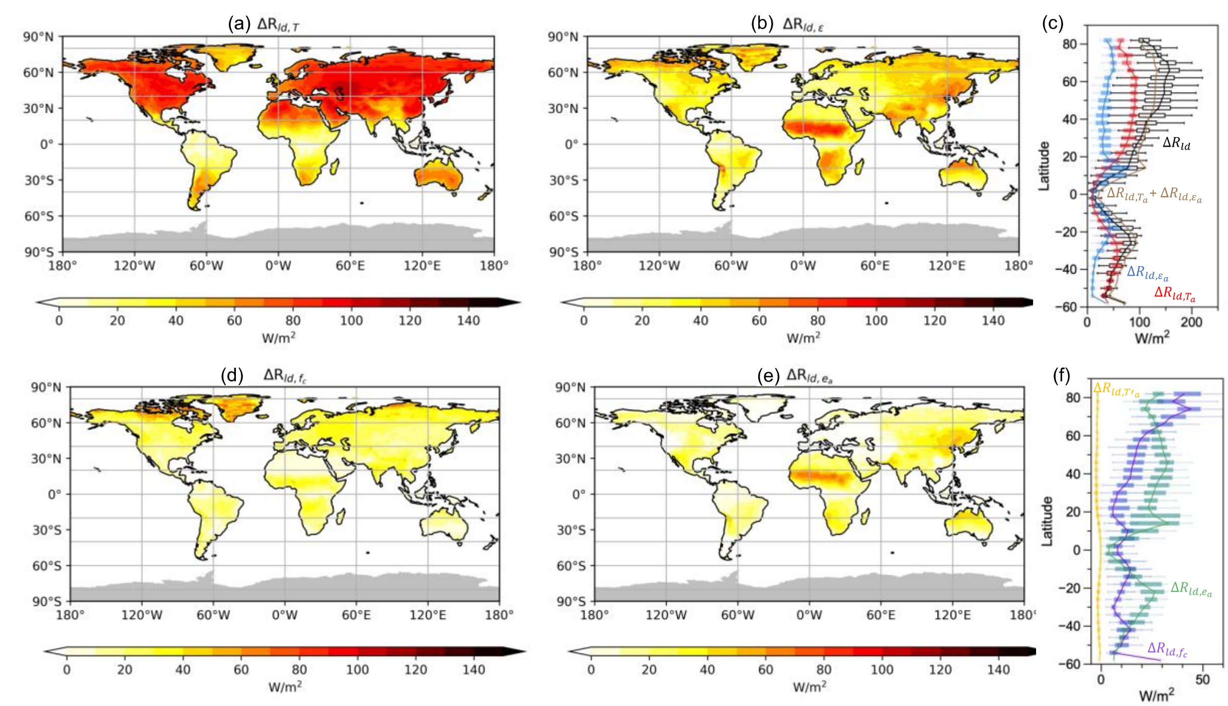

Figure 5. Decompositions of the mean seasonal variation (Δ, difference between the maximum and minimum monthly data at each grid) of R_{ld} in the NASA-CERES dataset into contributions by (a) lower atmospheric heat storage ($\Delta R_{ld,T}$) and (b) emissivity ($\Delta R_{ld,\varepsilon}$), and (c) their latitudinal variations. Decomposed of $\Delta R_{ld,\varepsilon}$ into contributions by variations in (d) cloud cover ($\Delta R_{ld,f_c}$) and (e) humidity

($\Delta R_{ld,e_a}$), (f) their latitudinal variations. In Figs. a, b, d, e, grey shading indicates missing values. In Figs. c and f, the box shows the variation among the land grids at the same latitude, while the solid line is their mean. The upper and lower whisker indicate 95th and 5th percentiles, upper boundary, median line, and lower boundary of the box indicate the 75th, 50th, 25th quantiles, respectively.

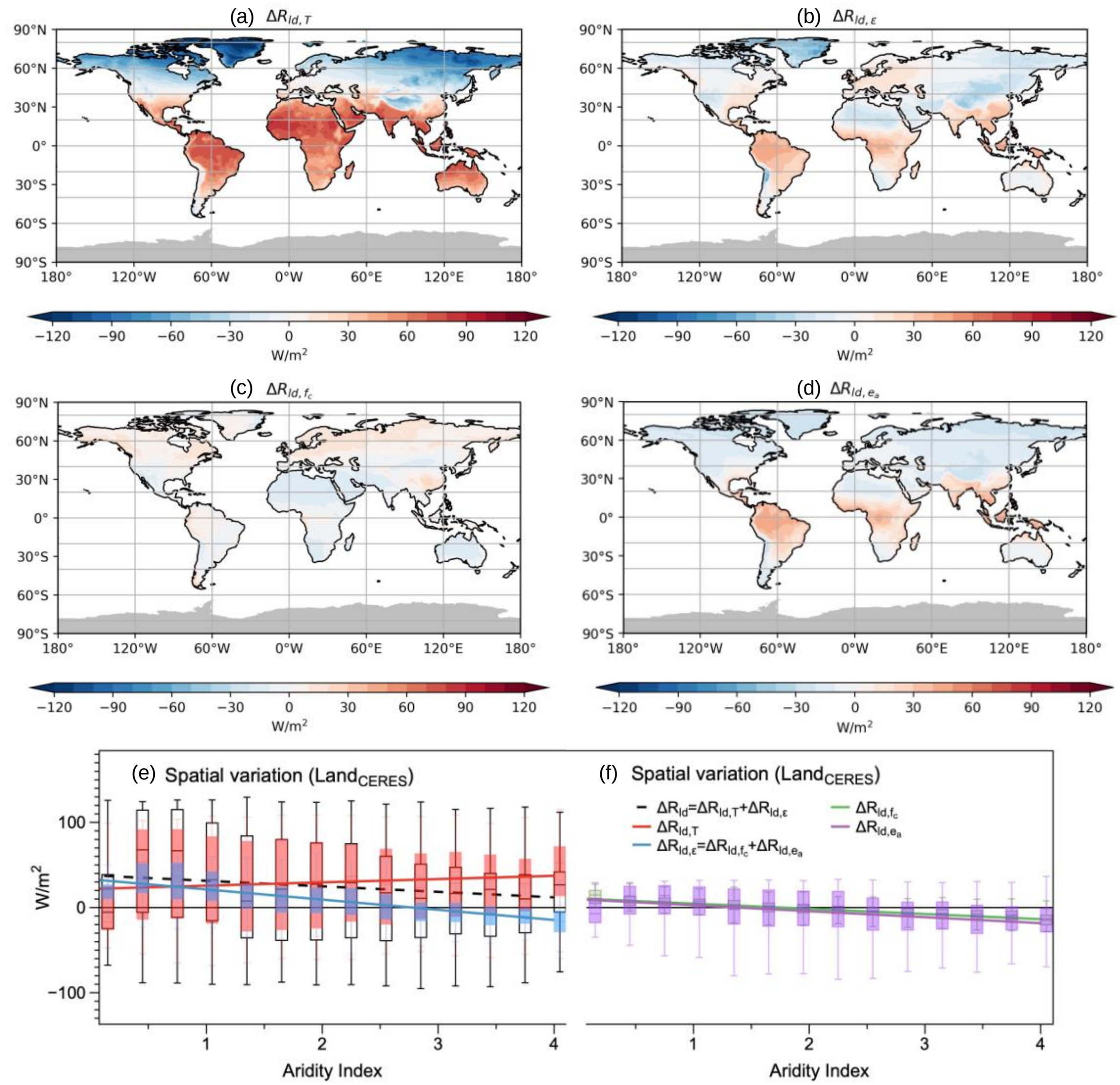

Figure 6. Decompositions of the multiyear-mean spatial variation of R_{ld} (deviations of the multiyear-mean value for each grid from the land-mean value) in the NASA-CERES dataset into contributions by (a) lower atmospheric heat storage ($\Delta R_{ld,T}$) and (b) emissivity ($\Delta R_{ld,\varepsilon}$). Decomposition of $\Delta R_{ld,\varepsilon}$ into contributions by (c) variations in cloud cover ($\Delta R_{ld,f_c}$) and (d) humidity ($\Delta R_{ld,e_a}$). Ins Figs. a-d, grey shading indicates missing values. In Figs. e and f, the box shows the variation among the land grids with the same aridity. The upper and lower whisker indicate 95th and 5th percentiles, upper boundary, median line, and lower boundary of the box indicate the 75th, 50th, 25th quantiles, respectively.